JGR Solid Earth

RESEARCH ARTICLE
10.1029/2020JB020728

Lithospheric Control of Melt Generation Beneath the Rungwe Volcanic Province, East Africa: Implications for a Plume Source

Emmanuel A. Njinju[1], D. Sarah Stamps[1], Kodi Neumiller[2], and James Gallager[2]

[1]Department of Geosciences, Virginia Tech, Blacksburg, VA, USA, [2]OPeNDAP, Narragansett, RI, USA

Key Points:

- Lithospheric modulated convection beneath the Rungwe Volcanic Province generates melt when mantle potential temperatures are elevated
- Plume material beneath the Rungwe Volcanic Province is required to explain geochemical and geophysical observations
- Lithospheric modulated convection enables the entrainment of plume material beneath the Rungwe Volcanic Province

Correspondence to:
E. A. Njinju,
njinju85@vt.edu

Citation:
Njinju, E. A., Stamps, D. S., Neumiller, K., & Gallager, J. (2021). Lithospheric control of melt generation beneath the Rungwe Volcanic Province, East Africa: Implications for a plume source. *Journal of Geophysical Research: Solid Earth*, *126*, e2020JB020728. https://doi.org/10.1029/2020JB020728

Received 5 AUG 2020
Accepted 7 APR 2021

Abstract The Rungwe Volcanic Province (RVP) is a volcanic center in an anomalous region of magma-assisted rifting positioned within the magma-poor Western Branch of the East African Rift (EAR). The source of sublithospheric melt for the RVP is enigmatic, particularly since the volcanism is highly localized, unlike the Eastern Branch of the EAR. Some studies suggest the source of sublithospheric melt beneath the RVP arises from thermal perturbations in the upper mantle associated with an offshoot of the African superplume flowing from the SW, while others propose a similar mechanism, but from the Kenyan plume diverted around the Tanzania Craton from the NE. Another possibility is decompression melting from upwelling sublithospheric mantle due to lithospheric modulated convection (LMC) where the lithosphere is thin. The authors test the hypothesis that sublithospheric melt feeding the RVP can be generated from LMC. We develop a 3D thermomechanical model of LMC beneath the RVP and the Malawi Rift and constrain parameters for sublithospheric melt generation due to LMC. We assume a rigid lithosphere and use non-Newtonian, temperature-, pressure-, and porosity-dependent creep laws of anhydrous peridotite for the sublithospheric mantle. We find a pattern of upwelling from LMC beneath the RVP. The upwelling generates melt only for elevated mantle potential temperatures (T_p), which suggests a heat source possibly from plume material. At elevated T_p, LMC associated decompression melts occurs at a maximum depth of ~150 km beneath the RVP. We suggest upwelling due to LMC entrains plume materials resulting in melt generation beneath the RVP.

1. Introduction

Melt intrusions into the lithospheric mantle and crust during extensional tectonics play a key role in weakening the lithosphere during magma-assisting rifting. Magma-assisted continental rifting involves magmatic intrusions that are sourced from melt generated in the sublithospheric mantle beneath the rift axis, which developed when mantle potential temperatures are higher than average (i.e., McKenzie & Bickle, 1988). The source of melt generation in the sublithospheric mantle beneath rifts has been proposed to originate from thermal perturbations due to plumes (e.g., Burke & Dewey, 1973; Furman et al., 2006; Saunders et al., 1992) or asthenospheric upwelling in response to thinned, extended lithosphere (e.g., Nielsen & Hopper, 2002; van Wijk et al., 2001; White & McKenzie, 1989).

The magma-poor Malawi Rift, which is the southernmost rift segment of the Western Branch of the East African Rift (EAR; Figure 1), provides a natural laboratory to investigate the source of asthenospheric melt. In particular, the source of sublithospheric melt for the Rungwe Volcanic Province (RVP), located in the northern region of the Malawi Rift, is contentious. Based on P- and S-wave seismic tomography, Grijalva et al. (2018) hypothesize deep melt beneath the RVP arises from flow of warm, mantle superplume material rising from the southwest that upwells beneath and diverts around the thick lithosphere of the Bangweulu cratonic block (Figure 1). In contrast, thermomechanical modeling by Koptev et al. (2018) suggests that the melt beneath the RVP is sourced from the Kenyan plume that is channeled into three mantle flows by the thick lithospheric keel of the Tanzanian craton and the Bangweulu cratonic block. Alternatively, Yu et al. (2020) suggest passive mantle upwelling distinct from plume sources explains upper mantle 3D seismic velocity and radial anisotropy structures. We hypothesize that the melt beneath the RVP is, at least, partly generated from decompression melting associated with the passive upwelling model.

The aims of this study are to investigate the sources of melt beneath the RVP by developing a 3D regional thermomechanical model of passive upwelling driven by lithospheric modulated convection (LMC) and

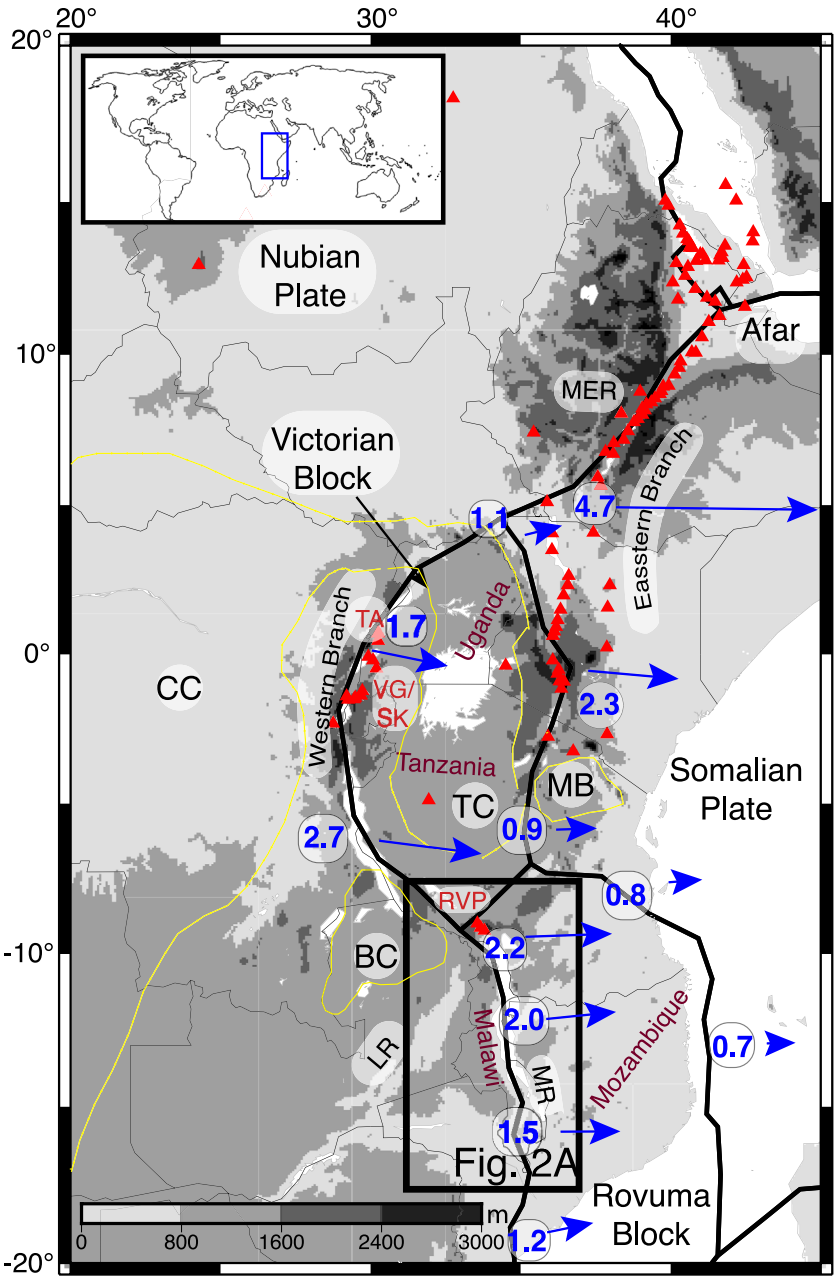

Figure 1. Digital elevation model (DEM) extracted from the Global 30 arc second Elevation Data (GTOPO30; DAAC, 2004) showing the Eastern and Western Branches of the East African Rift (EAR). The Eastern Branch of the EAR shows more volcanic centers (red triangles) than the Western Branch. The thin yellow lines outline cratons. MER = Main Ethiopian Rift. MB = Masai Block. BC = Bangweulu Craton. CC = Congo Craton. TC = Tanzanian Craton. MR = Malawi Rift. LR = Luangwa Rift. Red labels indicate volcanic centers in the Western Branch. TA = Toro Ankole. VG/SK = Virunga and South Kivu. RVP = Rungwe Volcanic Province. The black rectangle labeled Figure 2a indicates the study area shown in Figure 2a. Blue vectors are predicted velocities representing surface motion (mm/yr) relative to the Nubian Plate from Saria et al. (2014). Black thin lines delineate international borders with the names of the main countries transect by the Western Branch radiolabeled in brown colors. The inset map shows the relative location of part of the EAR (blue rectangle) on Earth.

constrain the parameters required for sublithospheric melt generation due to LMC using the open-source finite element code ASPECT (Advanced Solver for Problems in Earth's ConvecTion; Bangerth et al., 2018a; Bangerth et al., 2018b; Heister et al., 2017; Rose et al., 2017). LMC is sublithospheric mantle convection generated from temperature variations due to lateral variations in lithospheric thickness. An isotherm is

assumed for the base of the lithosphere with an approximate adiabatic increase in temperature below the lithosphere. The model takes into account rheological flow laws that allow for the generation of sublithospheric melts in a continental setting.

This study is part of the EarthCube project BALTO (Brokered Alignment of Long-Tail Observations), which is aimed at developing new, state-of-art cyberinfrastructure that enables brokered access to diverse geoscience datasets. One of the BALTO developments is a new plug-in for the community extensible National Science Foundation (NSF) open-source finite element code ASPECT that permits the user to access data over the internet using web services from any remote server that uses DAP (Data Access Protocol; Gallagher et al., 2004; Neumiller et al., 2020). This study is a use-case of this BALTO cyberinfrastructure, which accesses lithospheric thickness (Fishwick et al., 2010 updated) to constrain LMC and calculate melt generation beneath the RVP and the Malawi Rift.

LMC has a pattern of upwelling beneath the RVP where lithosphere is relatively thin and produces southern asthenospheric flow along the Malawi Rift. The upwelling from LMC is unable to generate melt except when potential temperatures of mantle are elevated. This result suggests that an additional heat source is present and is likely from plume materials because of the high $^{3}He/^{4}He$ detected in RVP lavas (Hilton et al., 2011). At elevated mantle potential temperatures, a significant percentage of sublithospheric melt from LMC occurs at depths of ~130–155 km localized beneath the RVP, consistent with the location and maximum depth (<200 km) of slow P-wave velocity anomalies beneath the RVP (Grijalva et al., 2018; Yu et al., 2020). These results suggest plume material is present, which explains available geochemical and geophysical observations of the RVP and the Malawi Rift. Sublithospheric melt beneath the RVP provides a source for shallow lithospheric intrusions of magma that weaken the lithosphere (e.g., Buck, 2006; Schmeling & Wallner, 2012) thereby enabling magma-assisted rifting in the northern Malawi Rift.

2. Tectonic Setting

2.1. The Malawi Rift

The Malawi Rift, which represents the southern prolongation of the Western Branch of the EAR (Figure 1), is a weakly extended rift (stretching factor of ~1.54; Njinju, Atekwana, et al., 2019) that spans ~900 km from southern Tanzania, through Malawi, to northern Mozambique. The Malawi Rift (Figure 2a) is characterized by asymmetric half grabens bounded by curvilinear border faults with records of deep seismicity suggesting that the border faults extend to the base of the crust (Craig et al., 2011; Ebinger et al., 2019). Indeed, geophysical studies reveal a thick crust (~38–45 km; Borrego et al., 2018; Njinju, Atekwana, et al., 2019) and a relatively strong and thick lithosphere beneath the central Malawi Rift (~115–210 km; Fishwick, 2010 updated; Njinju, Atekwana, et al., 2019). Geodetic studies suggest that the rift is opening at a surface velocity of 2.2 mm/yr in the north and 1.5 mm/yr in the south due to an eastward movement of the Rovuma Plate away from the Nubian Plate (Figure 1; i.e., Saria et al., 2014; Stamps et al., 2008; Stamps et al., 2020). The rift is largely magma-poor with volcanism limited to the Pliocene-Pleistocene RVP located in the northern tip of the rift (e.g., Fontijn et al., 2012; Furman, 2007). It is possible that magmatism beneath the RVP contributes to the relatively fast spreading rate of the northern segment of the Malawi Rift.

2.2. The Rungwe Volcanic Province

The RVP is the southernmost volcanic region in the Western Branch of the EAR (Figure 1), which lies at the northern tip of the Malawi Rift at the intersection of the Rukwa Rift and Usangu Rift, and covers approximately 1,500 km^2 (Figure 2b; Ebinger et al., 1989, 1997; Fontijn et al., 2012). The RVP comprises 3 large active volcanoes (Ngozi, Rungwe, and Kyejo; Figure 2b) in addition to more than 100 cones and domes (Fontijn et al., 2010; Harkin, 1960). The RVP lies at the nexus of three major border fault systems including the Livingstone fault of the Malawi Rift, Lupa fault of the Rukwa Rift, and the Usangu border faults, all of which have been active in Miocene-Recent times (Figure 2b; Fotijn et al., 2012).

The relationship between the tectonic structures in the region and magmatism remains controversial (Mesko et al., 2014; Roberts et al., 2012). Ebinger et al. (1989, 1993) suggest that volcanism in the RVP was synchronous with initial faulting and that local variations in the state-of-stress might result from plate

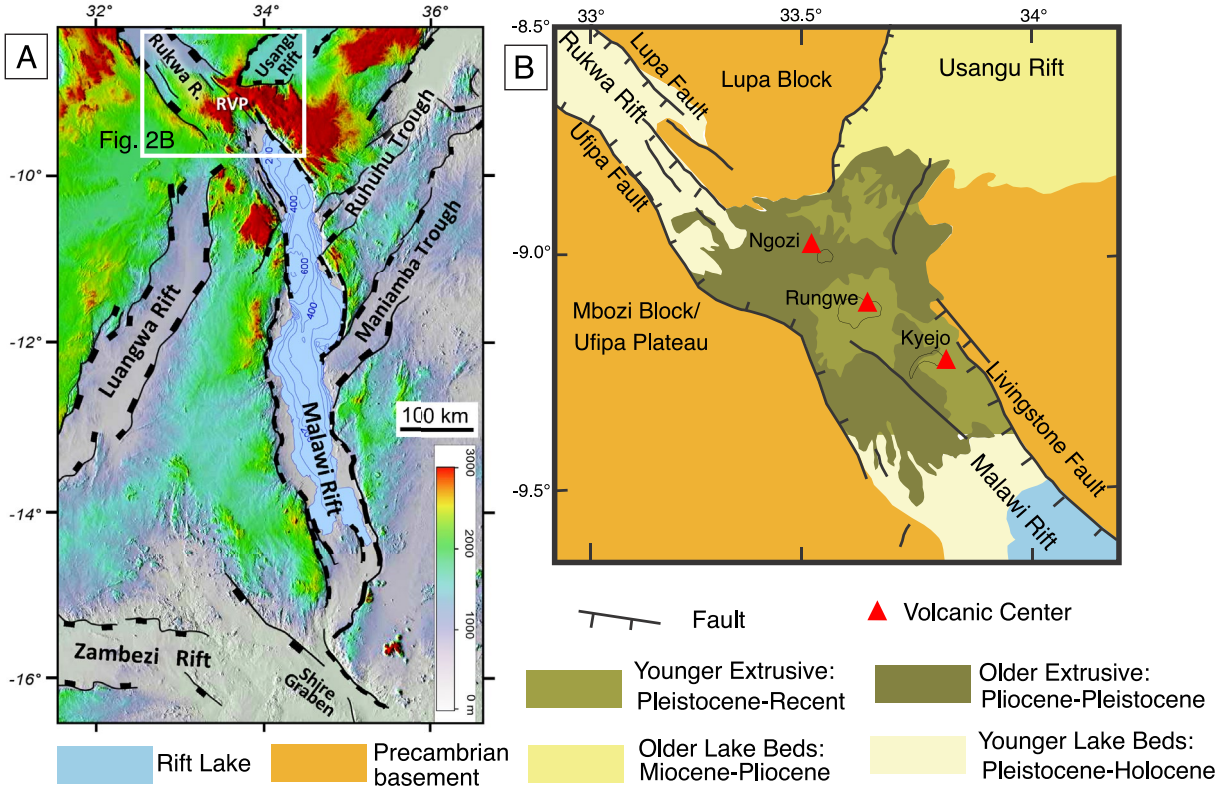

Figure 2. (a) Shuttle radar topography mission (SRTM) digital elevation model (DEM; Farr et al., 2007) of the Malawi Rift showing the border faults and the surrounding Paleozoic-Mesozoic Karoo rift basins corresponding to the study area (black rectangle) in Figure 1. Blue contour lines show water depth within Lake Malawi. The white box labeled Figure 2b in Figure 2a shows the location of Figure 2b. RVP = Rungwe Volcanic Province. (b) The geological map of the RVP and the surrounding Precambrian basement. Modified after Fotijn et al. (2012). The legend is referencing Figure 2b.

bending under the load of the volcanoes. Radiometric studies of samples from the RVP using $^{40}Ar/^{39}Ar$ dating techniques suggest that magmatism in the RVP started by 19 Ma (Mesko et al., 2014, 2020) and possibly as early as 25 Ma (Roberts et al., 2012). Although the onset of rifting in the Malawi and Rukwa Rifts is poorly known, Ebinger et al. (1993) used $^{40}Ar/^{39}Ar$ radiometric dating of samples from the RVP to suggest that faulting along the Livingstone border fault in the northern Malawi Rift started ~8.6 Ma. Moreover, U-Pb zircon ages of sediments from Lake Rukwa suggest reactivation and renewed subsidence in the Rukwa Rift at 8.7 Ma (Hilbert-Wolf et al., 2017). The ages of the RVP suggest that volcanism may predate the estimated onset of faulting along the Livingstone border fault and reactivation of the Rukwa Rift. Indeed, seismic studies by Grijalva et al. (2018) and Yu et al. (2020) image low velocity zones beneath the RVP, which suggest the thermal weakening of the lithosphere (with associated magmatism). Thermomechanical modeling by Koptev et al. (2018) suggest that the magmatism beneath the RVP may precede rift-related fault development.

The source of the magma beneath the RVP still remains enigmatic. Studies by Grijalva et al. (2018) and Koptev et al. (2018) suggest the presence of a mantle plume material beneath the RVP that generates melt. This hypothesis is supported by geochemical evidence from RVP lavas showing elevated mantle potential temperatures (Rooney et al., 2012) and elevated $^{3}He/^{4}He$ isotopic ratios (Hilton et al., 2011). However, Yu et al. (2020) suggest that the melt beneath the RVP arises from decompression melting in response to passive upwelling associated with lithospheric stretching based on relatively shallow low seismic velocity anomalies. Our study tests these hypotheses.

3. Methods

We simulate time-dependent LMC that incorporates melt generation in the sublithospheric mantle in a 3D domain using the finite element code ASPECT (Bangerth et al., 2018a, 2018b; Heister et al., 2017; Rose et al., 2017) to test the potential role of LMC in sublithospheric melt generation beneath the RVP and the Malawi Rift. Recent studies demonstrate the capabilities of modeling melt generation and magma dynamics in ASPECT (Dannberg et al., 2019; Dannberg & Heister, 2016), however this is the first study that uses present-day lithospheric structure as input to model melt generation associated with LMC.

3.1. 3D Lithospheric Modulated Convection Modeling

3.1.1. Governing Equations

We generate LMC beneath the Malawi Rift by solving for the velocity term $\boldsymbol{u}$ in the conservation equation for momentum (Equation 1) and mass (Equation 2) for an incompressible fluid:

$$-\nabla\cdot\left[2\eta\,\varepsilon(\boldsymbol{u})\right]+\nabla p=\rho\boldsymbol{g}\qquad in\,\Omega, \tag{1}$$

$$\nabla\cdot\boldsymbol{u}=0\qquad in\,\Omega, \tag{2}$$

where $\varepsilon(\boldsymbol{u})$, p, η, ρ, and $\boldsymbol{g}$ is, respectively, the strain rate, total pressure (sum of the lithostatic and dynamic pressure), viscosity, density, and gravitational acceleration. In order to model melt generation, we also simulate changes in temperature caused by heat transfer in the model by solving the energy conservation equation (Equation 3). We apply the extended Boussinesq approximation that includes shear heating, adiabatic heating, and latent heat of melting in the heating model (Christensen & Yuen, 1985):

$$\begin{aligned}\rho_0 C_p\left(\frac{\partial T}{\partial t}+\boldsymbol{u}\cdot\nabla T\right)-\nabla\cdot k\nabla T &= 2\eta\left[\varepsilon(\boldsymbol{u}):\varepsilon(\boldsymbol{u})\right]\\ &+\alpha T\left(\boldsymbol{u}\cdot\nabla p\right)\\ &+\rho_0 T\Delta S\left(\frac{\partial F}{\partial t}+\boldsymbol{u}\cdot\nabla F\right)\qquad in\,\Omega\end{aligned} \tag{3}$$

where C_p is the specific heat, α is the thermal expansivity, and k is the thermal conductivity. We assume a uniform crustal thickness of 30 km in the model with an average thermal conductivity of k = 2.5 W.m^{-1}. K^{-1} (Njinju, Kolawole, et al., 2019) and a uniform density of 2,700 kg/m^3. For the lithospheric mantle, we assume an average thermal conductivity of 3.5 W.m^{-1}. K^{-1} (Burov, 2011; Koptev et al., 2018) and a uniform density of 3,300 kg/m^3. We assume a thermal conductivity of 4.7 W.m^{-1}. K^{-1} for the sublithospheric mantle (Clauser & Huenges, 1995; Dannberg & Heister, 2016). However, the effective density of partially molten rocks (ρ_{eff}) in the sublithospheric mantle is given by:

$$\rho_{eff}=\rho_{solid}-F\left(\rho_{solid}-\rho_{melt}\right) \tag{4}$$

where F is the melt fraction (see Section 3.2), the density of solid rock ρ_{solid} and the density of melt ρ_{melt} vary with both temperature and pressure as follows:

$$\rho_{solid,melt}=\rho(T,p)=\rho_0\left[1-\alpha\left(T-T_0\right)\right]e^{\left[\beta\left(p-p_0\right)\right]} \tag{5}$$

where β is the compressibility coefficient, ρ_0 is the reference density at reference temperature T_0 and reference pressure p_0. ρ_0 = 3,300 kg/m^3 for solid rocks and ρ_0 = 3,000 kg/m^3 for melts. We do not model phase changes in the mantle transition zone. We normalize the pressure to a surface pressure of $p_0 = 10^5$ Pa where T_0 = 293 K (Yang et al., 2018). For the Earth's mantle, $\alpha = 3\times10^{-5}$ K^{-1}, C_p = 1250 J.kg^{-1}. K^{-1}, and $\beta = 4.2\times10^{-12}$ Pa^{-1}. The latent heat consumed during melting is proportional to the melting rate

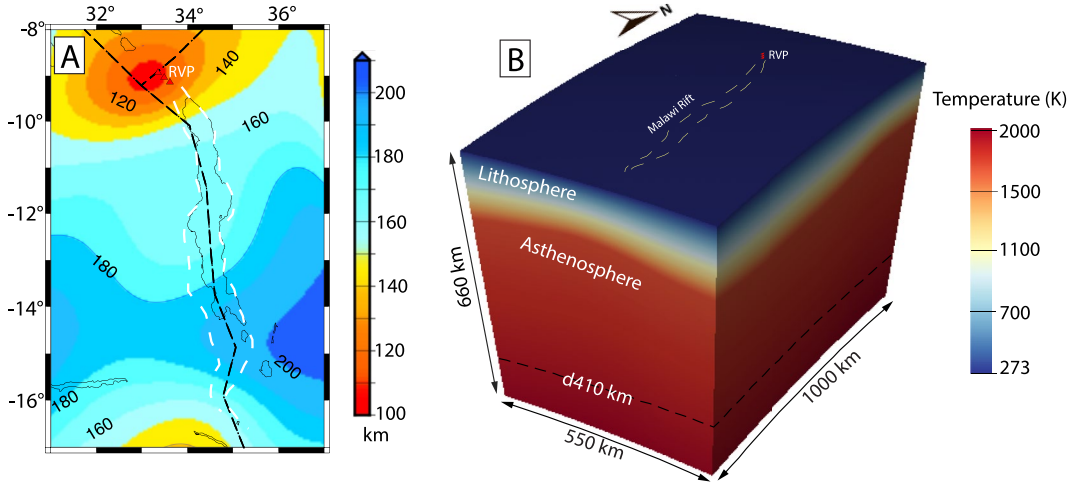

Figure 3. (a) Lithospheric thickness map of the Malawi Rift and surroundings, updated from Fishwick (2010) which we use as input in this study. The blue contours show lines of equal lithospheric thickness at 20 km intervals. Black dotted lines represent plate boundaries from Stamps et al. (2008). White dotted lines indicate the outline of the Malawi Rift traced from the shuttle radar topography mission (SRTM) digital elevation model (DEM) (Figure 2a; Farr et al., 2007). (b) Numerical model setup showing the model dimensions and the initial temperature condition as the background in 3D. Yellow dotted lines show the outline of the Malawi Rift. RVP = Rungwe Volcanic Province.

$\Gamma = \rho_0 \left(\frac{\partial F}{\partial t} + \boldsymbol{u} \cdot \nabla F \right)$ and the entropy change ΔS. The latent heat of melting is incorporated, with an entropy change of $\Delta S = -300$ J.kg^{-1}. K^{-1} (Dannberg & Heister, 2016).

3.1.2. Model Setup

Our model domain has dimensions of 550 × 1,000 × 660 km along latitude, longitude, and depth, respectively, for a spherical chunk geometry (Figure 3b). However, our regions of interest beneath the RVP and the entire Malawi Rift are distant from the model boundaries so that boundary effects are limited. Based on previous tests of edge-effects on the interior of the model due to different velocity boundary conditions (free slip vs. zero velocity; Njinju, Atekwana, et al., 2019); we set the velocities at all the sides of the model to zero which exerts minimal edge-effects on the model interior from the boundaries of the model. We do not impose plate velocities because we are focused on modeling Poiseuille's flow which we call LMC in this case, rather than Couette flow due to plate motion. Moreover, we are using realistic constraints of the lithospheric structure and want to avoid deforming the lithosphere. We refine the entire model domain to a global mesh refinement of 6 such that each element is ~8 × 15 × 10 km with 17.5 million unknowns computed on 120 cores. The model is comprised of a lithosphere and an underlying sublithospheric mantle that extends to 660 km depth.

The lithospheric structure is read from the BALTO site by the BALTO-ASPECT plugin using the web services provided by the BALTO broker. The lithosphere is part of the updated lithospheric structure model of Fishwick (2010) mapped into the 3D domain for the Malawi Rift and surroundings (Figure 3a). The lithosphere is thinnest beneath the RVP at the northern tip of the Malawi Rift (~100 km) and also beneath the southern rift segment (~100–125 km). The lithosphere is thickest beneath the central segment of the Malawi Rift (~175–200 km). The lithospheric structure produces lateral variations in temperature and pressure such that relatively thin lithosphere has hotter geothermal gradients and lower overburden pressure than the thicker lithosphere, which is relatively colder and exerts a higher lithostatic pressure. The temperature and pressure variations due to variations in the lithospheric thickness lead to lateral density perturbations in the sublithospheric mantle that drive LMC (Equations 4,5).

The initial temperature structure (Figure 3b) includes an approximation of a conductive geotherm for the lithosphere with a linear temperature gradient from the surface ($T_0 = 293$ K) to the base of the lithosphere. The base of the lithosphere is an isotherm defined by the mantle potential temperature T_p below which

the temperature increases approximately adiabatically (0.4 K/km) until it reaches the base of the model at 660 km where the temperature is fixed over time, but laterally varying. This initial temperature condition (Figure 5) results in lateral temperature variations throughout the model with the relatively coolest temperatures beneath thick lithosphere regions. The mantle potential temperature, T_p is the temperature that the mantle would have at the surface if ascended along an adiabat without melting (McKenzie & Bickle, 1988). The T_p in the RVP from eruptions occurring in the past 10 Ma ranges from ~1,420 to 1,450°C (~1,693–1,723 K) based on the geochemical observations of Rooney et al. (2012). We test a range of T_p (1,693–1,800 K) and find that T_p = 1,800 K produces a geotherm hot enough to generate melt (see Section 3.3.1). The temperature boundary conditions are given by fixed temperatures at the surface and bottom of the model with zero heat flux at the sides of the model. The surface temperature is fixed at 293 K while the temperature at the base of the model varies laterally in temperature but remains fixed with time.

3.1.3. Rheology

Mantle convection is highly dependent on the viscosity. Since we are interested in LMC in the sublithospheric mantle, we impose a strong, uniform viscosity of 10^{23} Pa.s for the lithosphere (Figures 4a and 4b). For the sublithospheric mantle, we use non-Newtonian, temperature-, pressure- and porosity-dependent creep laws of anhydrous peridotite. Unlike the viscosity model of Keller et al. (2013), which is given by the application of an exponential melt-weakening factor to a constant background mantle viscosity of 10^{22} Pa.s, we assume the background viscosity of the sublithospheric mantle is governed by composite rheology for dry olivine material parameters (Jadamec & Billen, 2010). The composite rheology (η_{comp}) is the effective value of the viscosity from dislocation-creep (η_{disl}) and diffusion-creep (η_{diff}) flow laws of dry olivine and is given by:

$$\eta_{diff,disl} = \frac{1}{2} A^{-\frac{1}{n}} d^{\frac{m}{n}} \dot{\epsilon}^{\frac{1-n}{n}} exp\left(\frac{E_a + pV_a}{nRT}\right) \tag{6}$$

$$\eta_{comp} = \frac{\eta_{diff} \times \eta_{disl}}{\eta_{diff} + \eta_{disl}} \tag{7}$$

where A is the prefactor, n is the stress exponent, $\dot{\epsilon}$ is the square root of the second invariant of the deviatoric strain rate tensor, d is the grain size, m is the grain size exponent, E_a is the activation energy, V_a is the activation volume, p is pressure, R is the gas constant, and T is the temperature. The values for the parameters A, n, m, E_a, and V_a are obtained from experimental studies of dry olivine (Hirth & Kohlstedt, 2004, Table 1). The viscosity of the sublithospheric mantle ($\eta_{sublith\text{-}mantle}$) with porosity dependence is given by:

$$\eta_{sublith-mantle} = \eta_{comp} \times e^{\left[-\alpha_\phi \phi\right]} \tag{8}$$

where the exponential melt-weakening factor is experimental-constrained to $25 \leq \alpha_\Phi \leq 30$ (Mei et al., 2002). We use the average value of $\alpha_\Phi = 27.5$. The porosity Φ is simply the melt fraction, or the volume fraction, of peridotite that is already molten. The material properties for each layer (lithosphere and sublithospheric mantle) are defined by compositional fields. The compositional fields for the lithosphere include "crust" and "lithospheric mantle," while the sublithospheric mantle is divided into two compositional fields called "porosity" and "peridotite." Partial melt in the model is tracked through the compositional field called "porosity." The viscosity at each quadrature point is calculated from the effective value of the viscosity of the compositional fields weighted by the volume fraction of each composition at the same location (Figures 4a and 4b; Rajaonarison et al., 2020).

Setting the velocities at the bottom boundary to zero approximates the effect of the high viscosity jump across the transition zone on slowing mantle flow velocities (410–660 km; Ballmer et al., 2007; Rajaonarison et al., 2020).

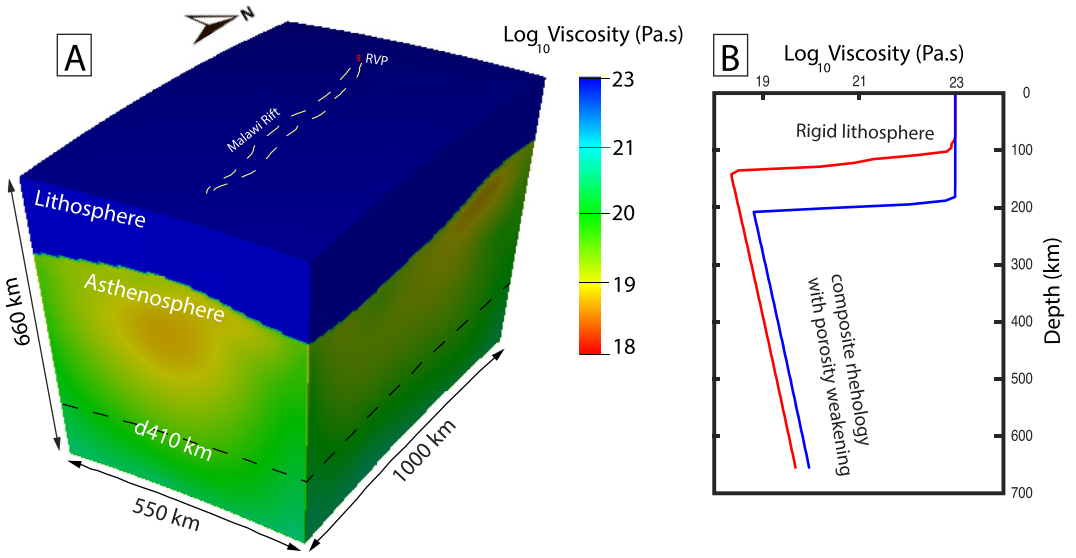

Figure 4. (a) Three-dimensional representation of the initial viscosity field. Yellow dotted lines show the outline of the Malawi Rift. RVP = Rungwe Volcanic Province. (b) One-dimensional initial viscosity depth profiles for a lithospheric thickness of 100 km (red) and 200 km (blue).

3.2. Partial Melting

For efficient modeling of melt generation in the sublithospheric mantle, we model low extent melting of anhydrous peridotite, particularly lherzolite, which occurs prior to the exhaustion of clinopyroxene. We use the melting parameterization of Katz et al. (2003), which is valid for shallow upper mantle melting beneath

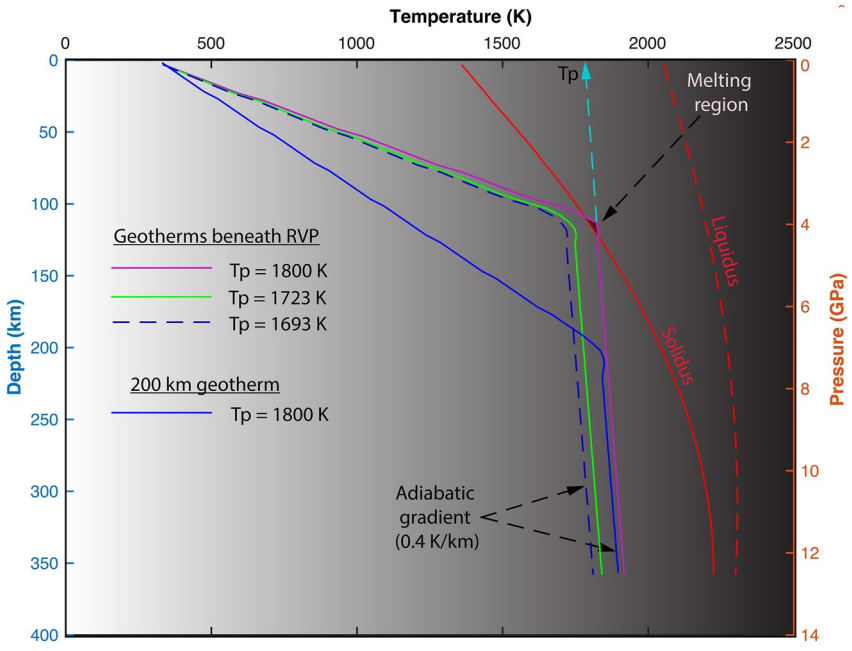

Figure 5. A combined plot of temperature-depth profiles (blue solid lines for a 100 km thick lithosphere and blue-dashed lines for a 200 km thick lithosphere) and a pressure-temperature phase diagram depicting shallow melting of anhydrous peridotite parameterized from Katz et al. (2003). The red solid line represents the solidus (0% melt) and the red-dashed line represents the liquidus (100% melt). The solidus and liquidus are plotted from Equations 9b and 9c respectively. T_p represents the mantle potential temperature.

Table 1
Rheological Parameters for Dry Olivine Used in the Viscosity Flow Law of the Sublithospheric Mantle

Parameter	Symbol	Dislocation creep	Diffusion creep	Unit
Activation energy	E_a	530×10^3	375×10^3	J/mol
Activation volume	V_a	18×10^{-6}	6×10^{-6}	m^3/mol
Grain size	d	-	10×10^{-3}	m
Grain size exponent	m	-	3	-
Stress exponent	n	3.5	1.0	-
Prefactor	A	7.4×10^{-15}	4.5×10^{-15}	$Pa^{-n}m^m s^{-1}$

The rheological parameters for the sublithospheric mantle are from Hirth and Kohlstedt (2003). The prefactor in Hirth & Kohlstedt (2004) (i.e., A′) is derived from uniaxial strain experiments and is converted to the plane strain equivalent (i.e., A) using the following relationship: $A = \frac{3^{\frac{n+1}{2}}}{2^{1-n}} \times 10^{-6(m+n)} A'$ for dry olivine (Becker, 2006).

continental lithosphere at pressures generally less than 13 GPa, which is the pressure at which the solidus temperatures is a maximum, that is, $-A_2/2A_3$ (Equation 9b). Partial melting in the sublithospheric mantle is highly dependent on the mantle potential temperature, T_p (Figure 5; McKenzie & Bickle, 1988), and will occur if the T_p is such that adiabatically ascending mantle intersects the solidus (Figure 5). The derived melt fraction $F(p, T)$ depends on the lithostatic pressure p (Pa) and temperature T (K) and is given by:

$$F\left(p,T\right) = \left(\frac{T - T_{solidus}}{T_{liquidus} - T_{solidus}}\right)^{1.5} \quad for \quad T_{solidus} \le T \le T_{liquidus} \tag{9a}$$

where the mantle solidus temperature $T_{solidus}$ and liquidus temperature $T_{liquidus}$ are respectively given by:

$$T_{solidus} = A_1 + A_2 p + A_3 p^2 \tag{9b}$$

$$T_{liquidus} = B_1 + B_2 p + B_3 p^2 \tag{9c}$$

where $A_1 = 1{,}085.7$ °C, $A_2 = 1.329 \times 10^{-7}$°C/Pa, $A_3 = -5.1 \times 10^{-18}$°C/$Pa^2$, $B_1 = 1{,}475.0$°C, $B_2 = 8.0 \times 10^{-8}$°C/Pa, and $B_3 = -3.2 \times 10^{-18}$°C/$Pa^2$.

We model batch melting, which is melting of an upwelling parcel of mantle rocks without instantaneous melt extraction (Asimow & Stolper, 1999; Ribe, 1985). Batch melting assumes that the melt fraction only depends on temperature and pressure and how much melt has already been generated at a given point, but not considering movement of melt in the melting parameterization. Although we do not model melt extraction by two-phase flow, the effect of latent heat release is switched off by setting the melt freezing rate to zero such that the latent heat term in Equation 3 turns off once the melting rate $\Gamma = \rho_0\left(\frac{\partial F}{\partial t} + \boldsymbol{u} \cdot \nabla F\right)$ (Equation 3) becomes negative due to downwelling and resultant cooling in the melting region. We simulate convection and batch melting for 20 Ma to ensure that steady state is achieved.

4. Results

4.1. Tests of Mantle Potential Temperatures and Lithospheric Thickness Variations in Melt Generation

Partial melting in the sublithospheric mantle occurs if the mantle potential temperature, T_p, is such that an adiabatically ascending mantle intersects the solidus. The derived melt fraction depends on the temperature and lithostatic pressure. The lithostatic pressure is constrained by the variations in the lithospheric thickness. Thin lithosphere exerts less of a mechanical barrier to adiabatic ascent (McKenzie & Bickle, 1988).

Therefore, partial melting in the sublithospheric mantle is highly dependent on T_p and lithospheric thickness variations.

4.1.1. Sensitivity Tests of Mantle Potential Temperature in Melt Generation During LMC

We use T_p to constrain the temperature at the base of the lithosphere. The T_p in the RVP ranges from ~1,420 to 1,450°C (~1,693–1,723 K) based on geochemical observations in Rooney et al. (2012). The geotherms for T_p = 1,623–1,723 K do not intersect the solidus (Figure 5) and so there is no decompression melt even after running the model for 20 Ma. For T_p = 1,800 K (1,527°C), the geotherm crosses the solidus (Figure 5) producing decompression melts. We further test a range of T_p values that are closer to 1,800 K (1,770, 1,780, 1,790, 1,800 K; Figure 6). For T_p = 1,770 K (blue lines, Figure 6), T_p = 1,780 K (yellow lines, Figure 6), T_p = 1,790 K (green lines, Figure 6), and T_p = 1,800 K (red lines, Figure 6), the geotherms cross the solidus producing initial decompression melts (~1.5%, ~3.4%, ~5.8%, and 8.5%, respectively) which decrease rapidly and cease before 2 Ma. The transient behavior of our melting model is likely due to a transient phase of adiabatic cooling while convection reaches steady state. For T_p = 1,800 K (red lines, Figure 6), the initial geotherm is hot enough such that as the model evolves to steady state, LMC generates the second stage of decompression melting when the adiabatic gradients within the active convection cell must have adjusted from the initial values.

4.1.2. Sensitivity Test of Lithospheric Thickness Variations in Melt Generation During LMC

Partial melting in the sublithospheric mantle is also highly dependent on the lithospheric thickness. This is because a thick lithosphere serves as a mechanical barrier to adiabatic ascent of hot mantle materials. The thickness of the melt zone and the maximum extent of partial melting are limited by the lithospheric thickness (e.g., McKenzie & O'Nions, 1995). We test the sensitivity of melt generation to lithospheric thickness variations in our model by conducting simulations with varied lithospheric thickness (+10 km and −10 km) based on the model of Fishwick (2010, updated). For T_p = 1,800 K, we find that when we increase the lithospheric thickness by 10 km (increase of mechanical barrier to adiabatic ascent of hot mantle materials), no melt is generated due to LMC (green line, Figure 7). However, when we reduce the lithospheric thickness by 10 km (reduction of mechanical barrier), an unrealistically high peak melt fraction (~12% melt; blue line, Figure 7) is generated from LMC beneath the RVP. For T_p = 1,723 K, reducing the lithospheric thickness by 10 km, generates a maximum instantaneous melt fraction of 0.04% (purple line, Figure 7). This test demonstrates that for LMC to generate decompression melt beneath the RVP, the mantle potential temperature must be highly elevated (T_p = 1,800 K). And that decompression melt beneath the RVP will occur at lower T_p, only if the lithospheric thickness is more than 10 km thinner than the lithospheric thickness model of Fishwick (2010, updated).

4.2. Lithospheric Modulated Convection

In our simulation, LMC develops spontaneously from our initial thermal conditions and forms where there is a transition in lithospheric thickness from relatively thick to thin (see Figure 3a). Figures 8a and 8b show flow patterns for T_p = 1,800 K at 17 Ma (time during which the flow is steady-state) resulting from our numerical modeling of LMC at 150 and 250 km depth slices, respectively. Sublithospheric mantle upwelling occurs beneath thin lithosphere, while downwelling occurs beneath relatively thick lithosphere. Our results indicate asthenospheric upwelling beneath the RVP driven by LMC. At 150 km depth (Figure 8a), asthenospheric upwelling (~1 cm/yr) with a diverging (~2 cm/yr) horizontal flow occurs only beneath the RVP where the lithosphere is thin (~100–120 km). At 250 km depth (Figure 8b), the asthenospheric upwelling beneath the RVP is faster (~3 cm/yr). Another zone of weaker upwelling (~0.5 cm/yr) occurs beneath the southern end of the Malawi Rift where the lithosphere is ~160 km thick compared to the thicker lithosphere (~180 km) in the central part of the rift. Our model suggests a southward flow of the upwelling mantle beneath the RVP toward the thick lithosphere in the central part of the Malawi Rift where the asthenospheric flow is characterized by downwelling (Figure 8b). The lithosphere, which is made rigid in the model, is not deforming.

4.3. Melt Generation

The time evolution of our melting model for T_p = 1,800 K (Figure 9) reveals two stages of melting. The first stage, which we call "the transient or unsteady melting state," occurs in the first 2 Ma of the model evolution

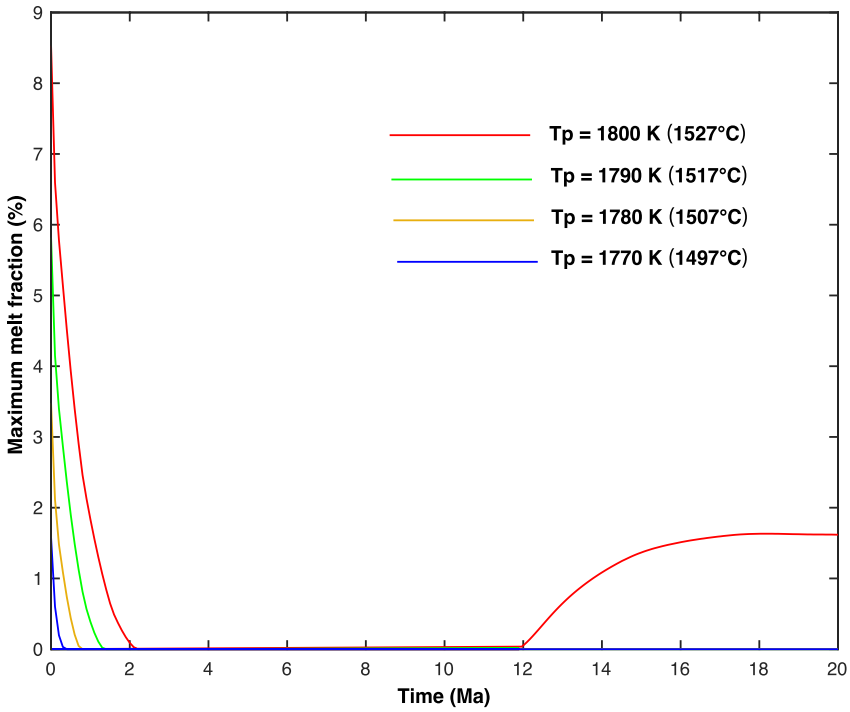

Figure 6. Sensitivity tests of mantle potential temperature in melt generation. A plot of melt fraction versus time showing the evolution of melt in the model for different mantle potential temperatures (T_p = 1,770, 1,780, 1,790, 1,800 K). No melt is generated for T_p = 1,693–1,723 K.

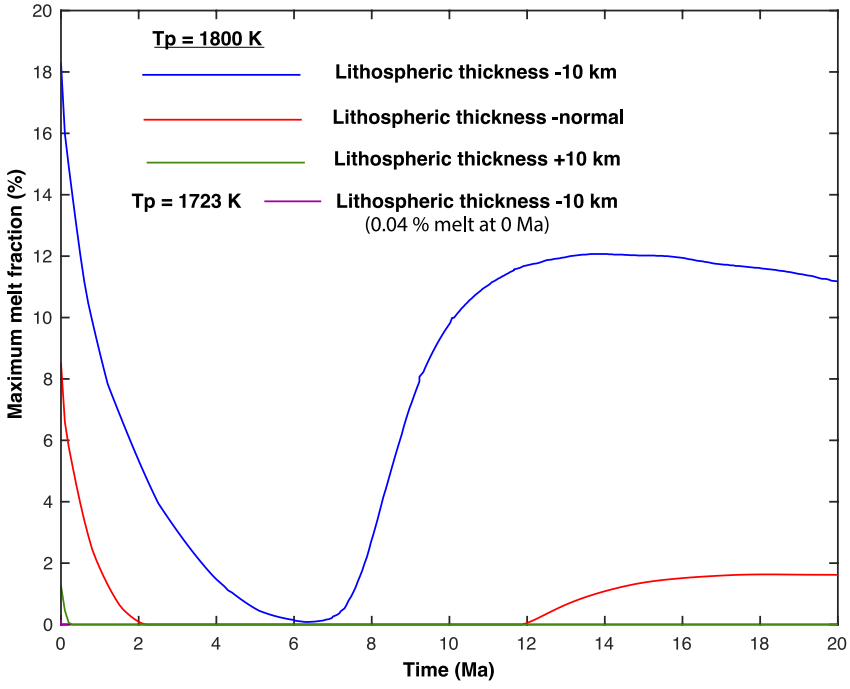

Figure 7. Sensitivity test of lithospheric thickness variation in melt generation for T_p = 1,800 K. Red lines show evolution of melt for a normal lithospheric thickness (Fishwick, 2010 updated). Blue line shows melt evolution after reducing the lithospheric thickness by 10 km. Green line shows the melt evolution after increasing the lithospheric thickness by 10 km. Although no melt is generated for a normal lithospheric thickness at T_p = 1,723 K, reducing the lithospheric thickness by 10 km (purple line) generates a maximum melt fraction of 0.04% at 0 Ma.

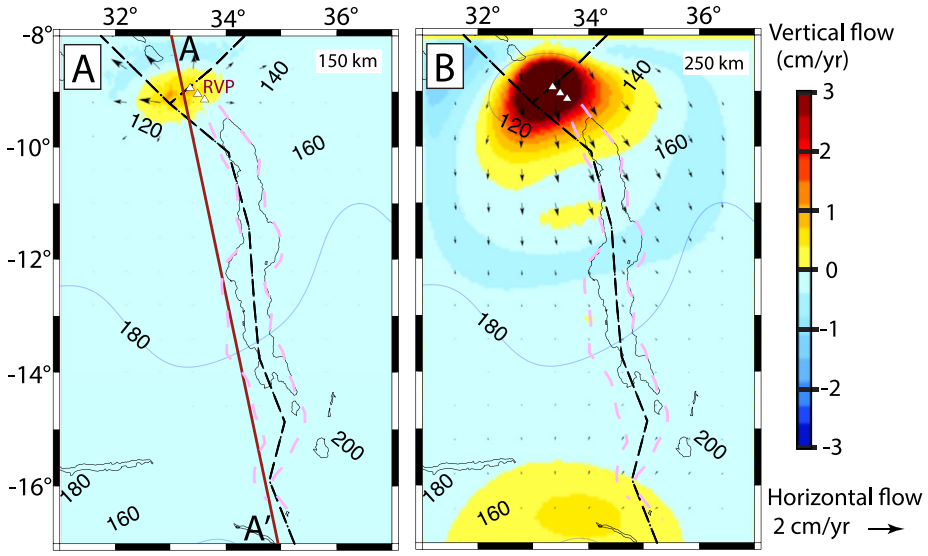

Figure 8. Depth slices showing lithospheric modulated convection beneath the RVP and the Malawi Rift at (a) 150 km and (b) 250 km depth at 17 Ma for mantle potential temperature, T_p = 1,800 (k) The vertical flow (background color) is overlain by the horizontal flow field (black arrows). Purple dotted lines indicate the outline of the Malawi Rift traced from the Shuttle Radar Topography Mission (SRTM) Digital Elevation Model (DEM; Farr et al., 2007, Figure 2a). White triangles represent the RVP. Black dotted lines delineate plate boundaries from Stamps et al. (2008). Blue contours show lines of equal lithospheric thickness at 20 km intervals from Fishwick (2010, updated). Brown profile AA′ in Figure 8a is the profile location for Figure 10.

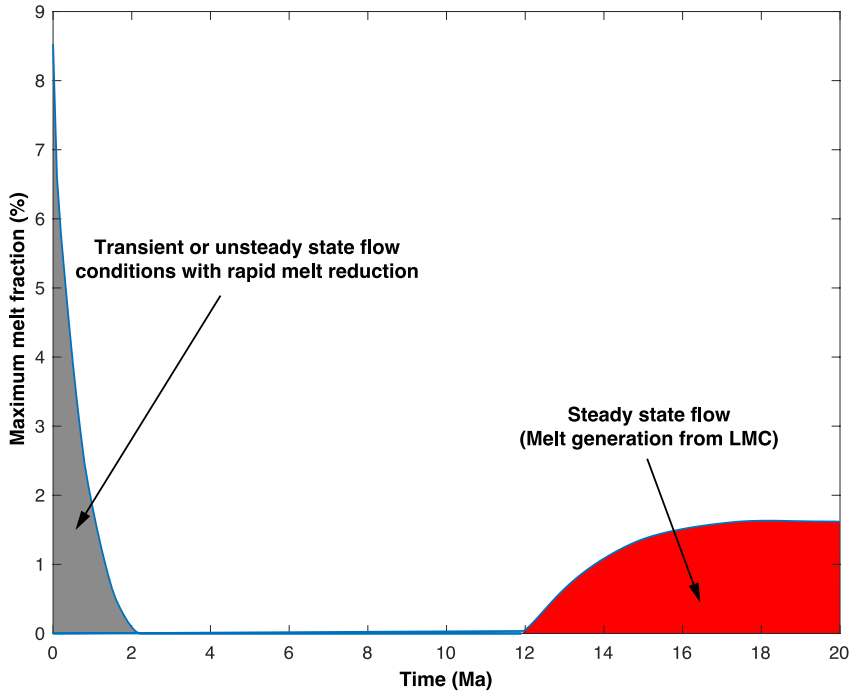

Figure 9. A plot of melt fraction versus time for T_p = 1,800 K showing the evolution of melt in the model. The gray color (0–2 Ma) represents when lithospheric modulated convection (LMC) is unstable and the initial decompression melt (~8.5%) generated from the initial temperature conditions decreases rapidly and ceases at 2 Ma. The red color (12–20 Ma) corresponds to melt generation.

beneath the RVP. The instantaneous (0 Ma) decompression melt (~8.5% melt) is not due to LMC; rather the melt arises from the initial conditions, which includes relatively thin lithosphere beneath the RVP and a high mantle potential temperature (T_p = 1,800 K). The endothermic melting process consumes latent heat and there is adiabatic cooling of upwelling mantle that rises to the melting region. The melting region thus experiences a net heat loss and progressively cools, such that melting sustained by intrinsic density variations decreases rapidly and ceases by 2 Ma (Ballmer et al., 2007). We suggest the second melting phase arises from LMC, which attains steady state at ~10 Ma after which the adiabatic gradients within the active convection cell have adjusted from the initial values. During this second stage of decompression melting that arises from LMC, the melt fraction increases rapidly from 0 to <1.5% between 12 and 16 Ma and saturates to 1.5% melt above 17 Ma (Figure 9).

Figures 10a–10c show time-variable LMC and melt generation for the melting parameterization of peridotite (Katz et al., 2003) across the RVP and the long axis of the Malawi Rift (profile AA′ defined in Figure 8a) for T_p = 1,800 K. The velocity fields show a similar mantle flow pattern at 10 Ma (Figures 10a), 17 Ma (Figure 10b), and 20 Ma (Figure 10c) with upwelling focused beneath the thin lithosphere of the RVP. The similar flow patterns from 10 to 20 Ma suggest that LMC is stable between 10 and 20 Ma. As described above, we suggest that at 10 Ma (Figure 10a) melt has yet to generate because of transient adiabatic cooling effects that occur while the convection field is reaching steady state. At 17 and 20 Ma (Figures 10b and 10c, respectively), upwelling from LMC has had enough time to transport deeper mantle materials to shallower depths, raising the sublithospheric geotherm above the mantle solidus temperature that leads to decompression melting of up to 1.5% melt fractions.

Depth slices of the melt model at 17 Ma for T_p = 1,800 K (Figures 11a–11d) indicates that melt generation due to LMC is restricted to depths of ~130–155 km beneath the RVP where the lithospheric thickness is < 120 km. The maximum melt fraction occurs at the center of the melting region (~145 km) with melt fractions reaching ~1.5% (Figures 11c).

5. Discussion

5.1. Sources of Deep Melt Beneath the Rungwe Volcanic Province

The most prominent feature in our model is the isolated region of sublithospheric mantle upwelling due to LMC beneath the RVP that is unable to generate decompression melt except when the mantle potential temperature is elevated (T_p = 1,800 K) suggesting that there is a heat source from plume material. In support of this hypothesis, a geochemical study of lava and tephra samples from the RVP by Hilton et al. (2011) shows significantly elevated values of helium isotope ratios ($^3He/^4He$) of 15 R_A (R_A = air $^3He/^4He$) which far exceeds typical upper mantle values. The high $^3He/^4He$ ratios associated with the RVP could be sourced from the primordial mantle in the core-mantle boundary brought to the surface by upwelling mantle plumes (Courtillot et al., 2003). Such plume-like $^3He/^4He$ ratios, suggest that mantle plume material contributes to the magmatism beneath the RVP. Geochemical study of geothermal fluids/gases in the RVP by Barry et al. (2013) suggest mid oceanic ridge-like $^3He/^4He$ and argue that the absence of hydrothermal samples in close proximity to high (plume-like) $^3He/^4He$ phenocryst localities could explain why plume-like $^3He/^4He$ ratios (>10 R_A) are not found in the fluid and gas samples.

For T_p = 1,800 K, decompression melt is generated beneath the RVP at depths of ~130–155 km with maximum melt fractions reaching ~1.5% (Figures 11c) which is consistent with melt fractions (1%–2% melt) beneath the Baikal Rift (Yang et al., 2018), which is a relatively magma-poor rift similar to the Malawi Rift. The melting region is spatially consistent with a pronounced low velocity anomaly (LVA) beneath the RVP imaged from P- and S-wave tomographic models developed by Grijalva et al. (2018). Similarly, Yu et al. (2020) used data recorded by seismic stations of the Seismic Array for African Rift Initiation experiment to develop a P-wave anisotropic tomography and found a LVA beneath the RVP that is mostly constrained to the sublithospheric mantle above 200 km depth. Grijalva et al. (2018) attribute the LVA beneath the RVP to the flow of warm, superplume mantle material from the southwest, upwelling beneath and around the Bangweulu Craton lithosphere. This result suggests that the LVA beneath the RVP may be a consequence of partial melts generated from plume material. Upwelling from LMC likely entrains the plume material into shallow

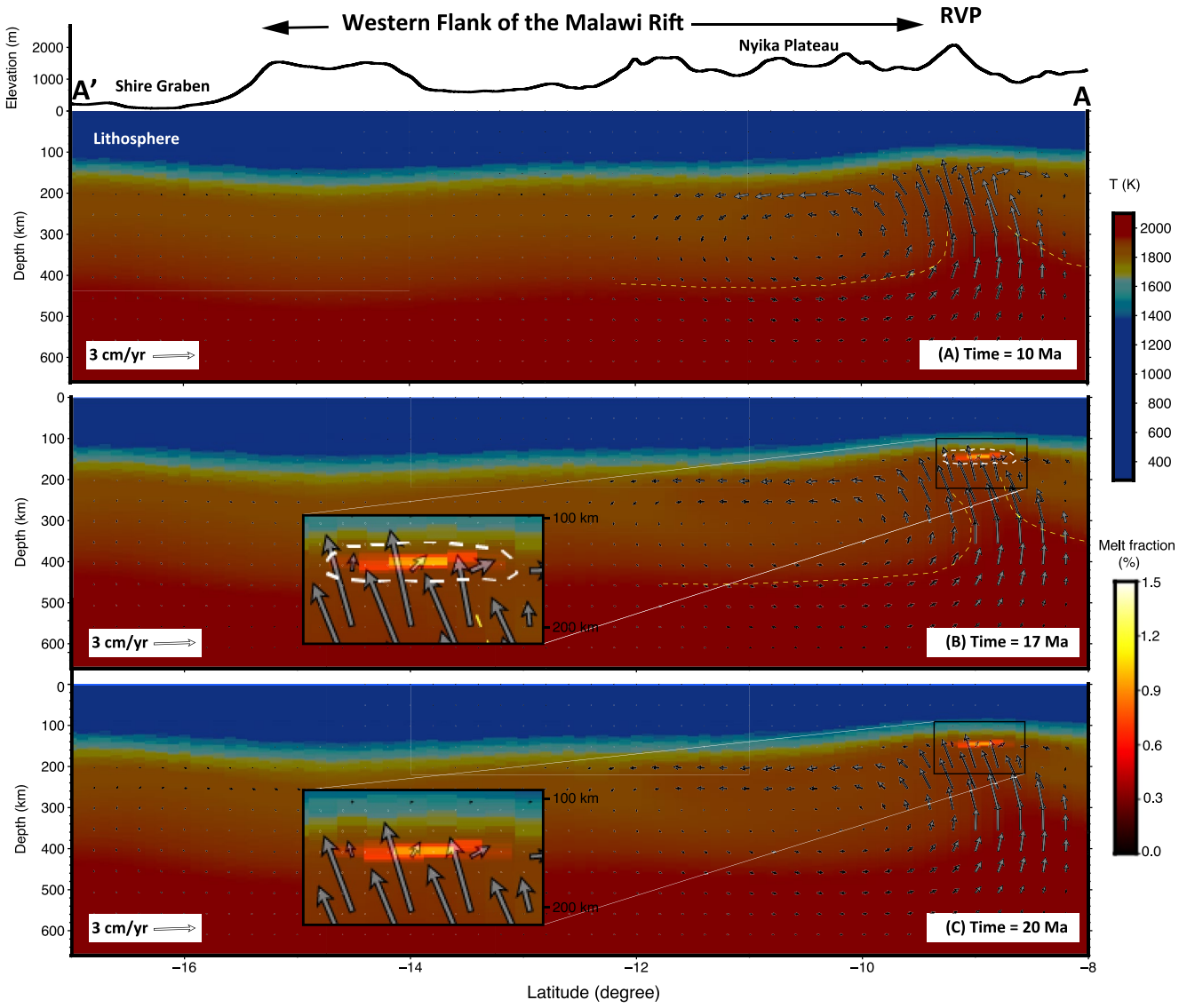

Figure 10. Profile showing time-dependent lithospheric modulated convection (LMC) across the Rungwe Volcanic Province (RVP) and the Malawi Rift (profile AA'; Figure 6a) for T_p = 1,800 (k): (a) Time = 10 Ma, (b) Time = 17 Ma, and (c) Time = 20 Ma. *Note*. The similarity in the structure of the mantle flow indicating steady-state LMC from 10 to 20 Ma. We include the yellow dotted lines to help visualize entrainment of deep, hot sublithospheric mantle rising to shallower depths beneath the lithosphere. Also, the melting regions in Figure 10b and 10c are zoomed-in for better visibility and shown as insets.

sublithospheric mantle beneath the RVP to generate melt. The melt that reaches the base of the lithosphere may refreeze, accumulate in a deep or shallow magma reservoir, inject into the lithosphere as dikes, or erupt to create new crust; however the fate of the melt in the lithosphere is beyond the scope of this study.

5.2. Implications for Incipient Rifting

Our numerical model of LMC reveals an isolated upwelling beneath the RVP where the lithosphere is thin. This upwelling beneath the RVP is unable to generate decompression melt except when the mantle potential temperature is elevated (T_p = 1,800 K). For T_p = 1,800 K, decompression meltoccurs beneath the RVP at depths of ~130–155 km which is supported by the presence of a LVA beneath the RVP that is mostly constrained to the upper mantle above 200 km depth (Grijalva et al., 2018; Yu et al., 2020). The sublithospheric melt may pond beneath the lithosphere and, subsequently, be injected into the mantle lithosphere and crust through preexisting lithospheric structures (Njinju, Atekwana, et al., 2019). Indeed, Accardo et al. (2020)

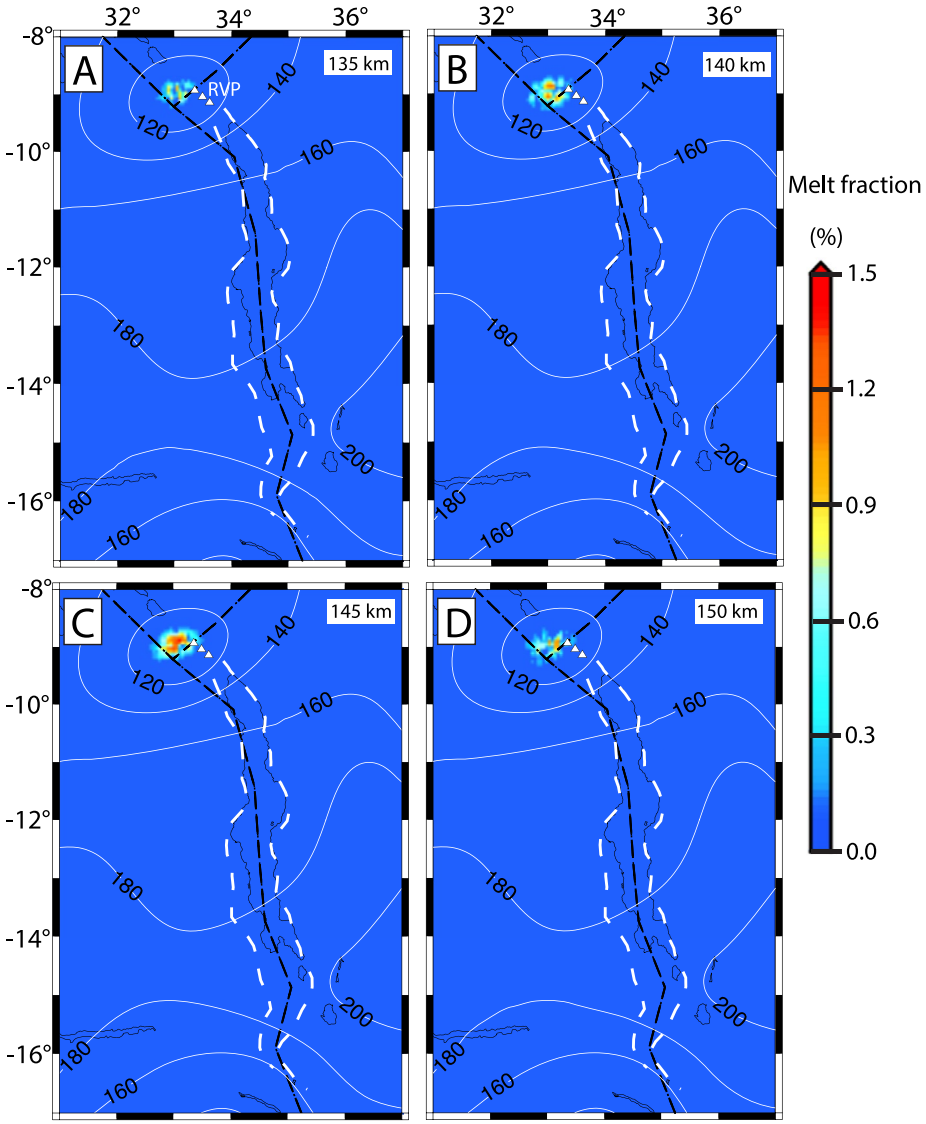

Figure 11. Depth slices showing melt fractions beneath the RVP and the Malawi Rift at (a) 135 km, (b) 140 km, (c) 145 km, and (d) 150 km depth at 17 Ma, for T_p = 1,800 (k). White dotted lines indicate the outline of the Malawi Rift traced from the shuttle radar topography mission (SRTM) digital elevation model (DEM; Farr et al., 2007, Figure 2a). White triangles represent the RVP. Black dotted lines delineate plate boundaries from Stamps et al. (2008). White contours show lines of equal lithospheric thickness at 20 km intervals from Fishwick (2010, updated).

used local measurements of Rayleigh-wave phase velocities to invert for shear wave velocities and clearly observed low velocities (<4.3 km/s) beneath the RVP at crust and upper mantle depths that are consistent with the presence of injected magma. The injection of magma into the lithosphere is an important factor in the process of continental rift initiation since magma can greatly reduce the strength of thick lithosphere and facilitates rifting (Bastow et al., 2011; Buck, 2006; Kendall et al., 2005; Kendall & Lithgow-Bertelloni, 2016; Schmeling & Wallner, 2012; Wallner & Schmeling, 2016). Recent seismic tomography models developed for the RVP and the northern Malawi Rift indicate that the lithosphere beneath the Malawi Rift may have been weakened prior to rifting (Accardo et al., 2020; Grijalva et al., 2018; Yu et al., 2020). Southward flow of the upwelling sublithospheric mantle beneath the RVP (Figure 8b) toward the Malawi Rift possibly leads to thermal erosion of the base of the lithosphere, thereby enabling localization of extension in the Malawi Rift (Njinju, Atekwana, et al., 2019).

6. Conclusions

Here, we investigate the sources of melt beneath the Rungwe Volcanic Province (RVP) by developing 3D thermomechanical models of LMC and constraining parameters for sublithospheric melt generation due to LMC. We assume a rigid lithosphere, while for the sublithospheric mantle we use non-Newtonian, temperature-, pressure- and porosity-dependent creep laws of anhydrous peridotite. Our LMC simulation is characterized by an isolated upwelling beneath the RVP where the lithosphere is relatively thin. The upwelling from LMC is unable to generate melt except for elevated mantle potential temperatures suggesting an additional heat source likely from plume material as supported by the high $^{3}He/^{4}He$ detected in RVP lavas. We, therefore, conclude that sublithospheric melt generated beneath the RVP results from elevated mantle potential temperatures associated with plume material and that sublithospheric mantle upwelling due to LMC enables the entrainment of this plume material to shallower depth beneath the RVP.

Data Availability Statement

The lithospheric thickness file can be accessed from the Hyrax server through the URL http://balto.opendap.org/opendap/lithosphere_thickness/. The mantle flow models are made available through the Open Science Framework repository with doi https://doi.org/10.17605/OSF.IO/NHFU2.

Acknowledgments
This project is supported by the NSF EarthCube Integration grant #1740704 and #1740627. Most of the figures in this paper were generated with Generic Mapping Tools V5.4.2 (Wessel et al., 2013). We also created some of the figures with VISIT v2.9 developed by the Lawrence Livermore National Laboratory. We thank the Computational Infrastructure for Geodynamics for supporting the development of ASPECT, which is funded by National Science Foundation Awards EAR-0949446 and EAR-1550901. We thank Editor Michael Bostock and Associate Editor Mark D. Behn for handling the manuscript and two reviewers: Dr. P. Barry and Dr. H. Schmeling for detailed and constructive comments.

References

Accardo, N. J., Gaherty, J. B., Shillington, D. J., Hopper, E., Nyblade, A. A., Ebinger, C. J., et al. (2020). Thermochemical modification of the upper mantle beneath the northern Malawi rift constrained from shear velocity imaging. *Geochemistry, Geophysics, Geosystems*, *21*(6), e2019GC008843. https://doi.org/10.1029/2019gc008843

Asimow, P. D., & Stolper, E. M. (1999). Steady-state mantle-melt interactions in one dimension: I. Equilibrium transport and melt focusing. *Journal of Petrology*, *40*(3), 475–494. https://doi.org/10.1093/petroj/40.3.475

Ballmer, M. D., Van Hunen, J., Ito, G., Tackley, P. J., & Bianco, T. A. (2007). Non-hotspot volcano chains originating from small-scale sublithospheric convection. *Geophysical Research Letters*, *34*(23). https://doi.org/10.1029/2007gl031636

Bangerth, W., Dannberg, J., Gassmoeller, R., & Heister, T. (2018a). *Aspect V2.0.1. Zenodo*. https://doi.org/10.5281/zenodo.1297145

Bangerth, W., Dannberg, J., Gassmoeller, R., Heister, T. (2018b). *Aspect: Advanced solver for problems in Earth's convection, user manual*. https://doi.arg/10.6084/m9.figshare.4865333

Barry, P. H., Hilton, D. R., Fischer, T. P., De Moor, J. M., Mangasini, F., & Ramirez, C. (2013). Helium and carbon isotope systematics of cold "mazuku" CO2 vents and hydrothermal gases and fluids from Rungwe Volcanic Province, southern Tanzania. *Chemical Geology*, *339*, 141–156. https://doi.org/10.1016/j.chemgeo.2012.07.003

Bastow, I. D., & Keir, D. (2011). The protracted development of the continent-ocean transition in Afar. *Nature Geoscince 4*(4), 248–250. https://doi.org/10.1038/ngeo1095

Becker, T. W. (2006). On the effect of temperature and strain-rate dependent viscosity on global mantle flow, net rotation, and plate-driving forces. *Geophysical Journal International*, *167*(2), 943–957. https://doi.org/10.1111/j.1365-246x.2006.03172.x

Borrego, D., Nyblade, A. A., Accardo, N. J., Gaherty, J. B., Ebinger, C. J., Shillington, D. J., et al. (2018). Crustal structure surrounding the northern Malawi rift and beneath the Rungwe Volcanic Province, East Africa. *Geophysical Journal International*, *215*(2), 1410–1426. https://doi.org/10.1093/gji/ggy331

Buck, W. R. (2006). The role of magma in the development of the Afro-Arabian Rift System. *Geological Society, London, Special Publications*, *259*(1), 43–54. https://doi.org/10.1144/gsl.sp.2006.259.01.05

Burke, K., & Dewey, J. F. (1973). Plume-generated triple junctions: key indicators in applying plate tectonics to old rocks. *The Journal of Geology*, *81*(4), 406–433. https://doi.org/10.1086/627882

Burov, E. B. (2011). Rheology and strength of the lithosphere. *Marine and Petroleum Geology*, *28*(8), 1402–1443. https://doi.org/10.1016/j.marpetgeo.2011.05.008

Christensen, U. R., & Yuen, D. A. (1985). Layered convection induced by phase transitions. *Journal of Geophysical Research*, *90*(B12), 10291–10300. https://doi.org/10.1029/jb090ib12p10291

Clauser, C., & Huenges, E. (1995). Thermal conductivity of rocks and minerals. *Rock physics and phase relations: A Handbook of Physical Constants*, *3*, 105–126.

Courtillot, V., Davaille, A., Besse, J., & Stock, J. (2003). Three distinct types of hotspots in the Earth's mantle. *Earth and Planetary Science Letters*, *205*(3–4), 295–308. https://doi.org/10.1016/s0012-821x(02)01048-8

Craig, T. J., Jackson, J. A., Priestley, K., & McKenzie, D. (2011). Earthquake distribution patterns in Africa: Their relationship to variations in lithospheric and geological structure, and their rheological implications. *Geophysical Journal International*, *185*(1), 403–434. https://doi.org/10.1111/j.1365-246x.2011.04950.x

DAAC, L. (2004). *Global 30 arc-second elevation data set GTOPO30*. Land Process Distributed Active Archive Center.

Dannberg, J., Gassmöller, R., Grove, R., & Heister, T. (2019). A new formulation for coupled magma/mantle dynamics. *Geophysical Journal International*, *219*(1), 94–107.

Dannberg, J., & Heister, T. (2016). Compressible magma/mantle dynamics: 3-D, adaptive simulations in ASPECT. *Geophysical Journal International*, *207*(3), 1343–1366. https://doi.org/10.1093/gji/ggw329

Ebinger, C., Djomani, Y. P., Mbede, E., Foster, A., & Dawson, J. B. (1997). Rifting archaean lithosphere: The Eyasi-Manyara-Natron rifts, East Africa. *Journal of the Geological Society*, *154*(6), 947–960. https://doi.org/10.1144/gsjgs.154.6.0947

Ebinger, C. J., Deino, A. L., Drake, R. E., & Tesha, A. L. (1989). Chronology of volcanism and rift basin propagation: Rungwe volcanic province, East Africa. *Journal of Geophysical Research*, *94*(B11), 15785–15803. https://doi.org/10.1029/jb094ib11p15785

Ebinger, C. J., Deino, A. L., Tesha, A. L., Becker, T., & Ring, U. (1993). Tectonic controls on rift basin morphology: Evolution of the Northern Malawi (Nyasa) Rift. *Journal of Geophysical Research*, *98*(B10), 17821–17836. https://doi.org/10.1029/93jb01392

Ebinger, C. J., Oliva, S. J., Pham, T. Q., Peterson, K., Chindandali, P., Illsley-Kemp, F., et al. (2019). Kinematics of active deformation in the Malawi Rift and Rungwe Volcanic Province, Africa. *Geochemistry, Geophysics, Geosystem*, *20*(8), 3928–3951. https://doi.org/10.1029/2019gc008354

Farr, T. G., Rosen, P. A., Caro, E., Crippen, R., Duren, R., Hensley, S., ..., & Seal, D. (2007). The shuttle radar topography mission. *Reviews of Geophysics*, *45*(2). https://doi.org/10.1029/2005rg000183

Fishwick, S. (2010). Surface wave tomography: Imaging of the lithosphere-asthenosphere boundary beneath central and southern Africa? *Lithos*, *120*(1), 63–73. https://doi.org/10.1016/j.lithos.2010.05.011

Fontijn, K., Ernst, G. G., Elburg, M. A., Williamson, D., Abdallah, E., Kwelwa, S., et al. (2010). Holocene explosive eruptions in the Rungwe volcanic province, Tanzania. *Journal of Volcanology and Geothermal Research*, *196*(1–2), 91–110. https://doi.org/10.1016/j.jvolgeores.2010.07.021

Fontijn, K., Williamson, D., Mbede, E., & Ernst, G. G. J. (2012). The Rungwe Volcanic Province, Tanzania - A volcanological review. *Journal of African Earth Sciences*, *63*, 12–31. https://doi.org/10.1016/j.jafrearsci.2011.11.005

Furman, T. (2007). Geochemistry of East African Rift basalts: An overview. *Journal of African Earth Sciences*, *48*(2–3), 147–160. https://doi.org/10.1016/j.jafrearsci.2006.06.009

Furman, T., Kaleta, K. M., Bryce, J. G., & Hanan, B. B. (2006). Tertiary Mafic Lavas of Turkana, Kenya: Constraints on East African Plume Structure and the occurrence of High-μ Volcanism in Africa. *Journal of Petrology*, *47*(6), 1221–1244. https://doi.org/10.1093/petrology/egl009

Gallagher, J., Potter, N., Sgouros, T., Hankin, S., & Flierl, G. (2004). *The data access protocol—DAP 2.0*. Retrieved from http://www.opendap.org/

Grijalva, A., Nyblade, A. A., Homman, K., Accardo, N. J., Gaherty, J. B., Ebinger, C. J., et al. (2018). Seismic evidence for plume- and craton-influenced upper mantle structure beneath the northern Malawi rift and the Rungwe volcanic province, East Africa. *Geochemistry, Geophysics, Geosystems*, *19*(10), 3980–3994. https://doi.org/10.1029/2018gc007730

Harkin, D. A. (1960). *The Rungwe volcanics at the northern end of Lake Nyasa*.

Heister, T., Dannberg, J., Gassmöller, R., & Bangerth, W. (2017). High accuracy mantle convection simulation through modern numerical methods - II: Realistic models and problems. *Geophysical Journal International*, *210*(2), 833–851. https://doi.org/10.1093/gji/ggx195

Hilbert-Wolf, H., Roberts, E., Downie, B., Mtelela, C., Stevens, N. J., & O'Connor, P. (2017). Application of U-Pb detrital zircon geochronology to drill cuttings for age control in hydrocarbon exploration wells: A case study from the Rukwa Rift Basin, Tanzania. *Bulletin*, *101*(2), 143–159. https://doi.org/10.1306/06281616003

Hilton, D. R., Halldórsson, S. A., Barry, P. H., Fischer, T. P., de Moor, J. M., Ramirez, C. J., & Scarsi, P. (2011). Helium isotopes at Rungwe Volcanic Province, Tanzania, and the origin of East African plateaux. *Geophysical Research Letters*, *38*(21). https://doi.org/10.1029/2011gl049589

Hirth, G., & Kohlstedt, D. (2004). Rheology of the upper mantle and the mantle wedge: A view from the experimentalists. *Inside the Subduction Factory*, *138*, 83–105.

Jadamec, M. A., & Billen, M. I. (2010). Reconciling surface plate motions with rapid three-dimensional mantle flow around a slab edge. *Nature*, *465*(7296), 338–341. https://doi.org/10.1038/nature09053

Katz, R. F., Spiegelman, M., & Langmuir, C. H. (2003). A new parameterization of hydrous mantle melting. *Geochemistry, Geophysics, Geosystems*, *4*(9). https://doi.org/10.1029/2002gc000433

Keller, T., May, D. A., & Kaus, B. J. P. (2013). Numerical modelling of magma dynamics coupled to tectonic deformation of lithosphere and crust. *Geophysical Journal International*, *195*(3), 1406–1442. https://doi.org/10.1093/gji/ggt306

Kendall, J.-M., & Lithgow-Bertelloni, C. (2016). Why is Africa rifting? *Geological Society, London, Special Publications*, *420*(1), 11–30. https://doi.org/10.1144/sp420.17

Kendall, J.-M., Stuart, G. W., Ebinger, C. J., Bastow, I. D., & Keir, D. (2005). Magma-assisted rifting in Ethiopia. *Nature*, *433*(7022), 146–148. https://doi.org/10.1038/nature03161

Koptev, A., Cloetingh, S., Gerya, T., Calais, E., & Leroy, S. (2018). Non-uniform splitting of a single mantle plume by double cratonic roots: Insight into the origin of the central and southern East African Rift System. *Terra Nova*, *30*(2), 125–134. https://doi.org/10.1111/ter.12317

Mckenzie, D., & Bickle, M. J. (1988). The volume and composition of melt generated by extension of the lithosphere. *Journal of Petrology*, *29*(3), 625–679. https://doi.org/10.1093/petrology/29.3.625

McKenzie, D., & O'NIONS, R. K. (1995). The source regions of ocean island basalts. *Journal of Petrology*, *36*(1), 133–159. https://doi.org/10.1093/petrology/36.1.133

Mei, S., Bai, W., Hiraga, T., & Kohlstedt, D. L. (2002). Influence of melt on the creep behavior of olivine–basalt aggregates under hydrous conditions. *Earth and Planetary Science Letters*, *201*(3–4), 491–507. https://doi.org/10.1016/s0012-821x(02)00745-8

Mesko, G. (2020). *Magmatism at the southern end of the East African Rift system: Origin and role during early-stage rifting*. (Doctoral dissertation). Columbia University.

Mesko, G., Class, C., Maqway, M., Boniface, N., Manya, S., & Hemming, S. (2014). The timing of early magmatism and extension in the southern east African rift: Tracking geochemical source variability with 40Ar/39Ar geochronology at the Rungwe volcanic Province, SW Tanzania. *Paper presented at the AGU Fall Meeting Abstracts*, V51A–V4730.

Neumiller, K., Gallagher, J., Njinju, E., & Stamps, D. S. (2020). *Remote data processing inside the ASPECT analysis tool*.

Nielsen, T. K., & Hopper, J. R. (2002). Formation of volcanic rifted margins: Are temperature anomalies required? *Geophysical Research Letters*, *29*(21), 18–21. https://doi.org/10.1029/2002gl015681

Njinju, E. A., Atekwana, E. A., Stamps, D. S., Abdelsalam, M. G., Atekwana, E. A., Mickus, K. L., et al. (2019). Lithospheric Structure of the Malawi Rift: Implications for magma-poor rifting processes. *Tectonics*, *38*(11), 3835–3853. https://doi.org/10.1029/2019tc005549

Njinju, E. A., Kolawole, F., Atekwana, E. A., Stamps, D. S., Atekwana, E. A., Abdelsalam, M. G., & Mickus, K. L. (2019). Terrestrial heat flow in the Malawi Rifted Zone, East Africa: Implications for tectono-thermal inheritance in continental rift basins. *Journal of Volcanology and Geothermal Research*, *387*, 106656. https://doi.org/10.1016/j.jvolgeores.2019.07.023

Rajaonarison, T. A., Stamps, D. S., Fishwick, S., Brune, S., Glerum, A., & Hu, J. (2020). Numerical modeling of mantle flow beneath Madagascar to constrain upper mantle rheology beneath continental regions. *Journal of Geophysical Research: Solid Earth*, *125*(2). Art-No. https://doi.org/10.1029/2019jb018560

Ribe, N. M. (1985). The generation and composition of partial melts in the earth's mantle. *Earth and Planetary Science Letters*, *73*(2–4), 361–376. https://doi.org/10.1016/0012-821x(85)90084-6

Roberts, E. M., Stevens, N. J., O'Connor, P. M., Dirks, P. H. G. M., Gottfried, M. D., Clyde, W. C., et al. (2012). Initiation of the western branch of the East African Rift coeval with the eastern branch. *Nature Geoscience 5*(4), 289–294. https://doi.org/10.1038/ngeo1432

Rooney, T. O., Herzberg, C., & Bastow, I. D. (2012). Elevated mantle temperature beneath East Africa. *Geology*, *40*(1), 27–30. https://doi.org/10.1130/g32382.1

Rose, I., Buffett, B., & Heister, T. (2017). Stability and accuracy of free surface time integration in viscous flows. *Physics of the Earth and Planetary Interiors*, *262*, 90–100. https://doi.org/10.1016/j.pepi.2016.11.007

Saria, E., Calais, E., Stamps, D. S., Delvaux, D., & Hartnady, C. J. H. (2014). Present-day kinematics of the East African Rift. *Journal of Geophysics Research: Solid Earth*, *119*(4), 3584–3600. https://doi.org/10.1002/2013jb010901

Saunders, A. D., Storey, M., Kent, R. W., & Norry, M. J. (1992). Consequences of plume-lithosphere interactions. *Geological Society, London, Special Publications*, *68*(1), 41–60. https://doi.org/10.1144/gsl.sp.1992.068.01.04

Schmeling, H., & Wallner, H. (2012). Magmatic lithospheric heating and weakening during continental rifting: A simple scaling law, a 2-D thermomechanical rifting model and the East African Rift System. *Geochemistry, Geophysics, Geosystems*, *13*(8). https://doi.org/10.1029/2012gc004178

Stamps, D. S., Calais, E., Saria, E., Hartnady, C., Nocquet, J. M., Ebinger, C. J., & Fernandes, R. M. (2008). A kinematic model for the East African Rift. *Geophysical Research Letters*, *35*(5). https://doi.org/10.1029/2007gl032781

Stamps, D. S., Kreemer, C., Fernandes, R., Rajaonarison, T. A., & Rambolamanana, G. (2020). Redefining East African Rift System kinematics. *Geology*. https://doi.org/10.1130/G47985.1

Van Wijk, J. W., Huismans, R. S., Ter Voorde, M., & Cloetingh, S. A. P. L. (2001). Melt generation at volcanic continental margins: No need for a mantle plume? *Geophysical Research Letters*, *28*(20), 3995–3998. https://doi.org/10.1029/2000gl012848

Wallner, H., & Schmeling, H. (2016). Numerical models of mantle lithosphere weakening, erosion and delamination induced by melt extraction and emplacement. *International Journal of Earth Sciences*, *105*(6), 1741–1760. https://doi.org/10.1007/s00531-016-1343-y

Wessel, P., Smith, W. H. F., Scharroo, R., Luis, J., & Wobbe, F. (2013). Generic mapping tools: Improved version released. *Eos Trans. AGU*, *94*(45), 409–410. https://doi.org/10.1002/2013eo450001

White, R., & McKenzie, D. (1989). Magmatism at rift zones: The generation of volcanic continental margins and flood basalts. *Journal of Geophysical Research*, *94*(B6), 7685–7729. https://doi.org/10.1029/jb094ib06p07685

Yang, H., Chemia, Z., Artemieva, I. M., & Thybo, H. (2018). Control on off-rift magmatism: A case study of the Baikal Rift Zone. *Earth and Planetary Science Letters*, *482*, 501–509. https://doi.org/10.1016/j.epsl.2017.11.040

Yu, Y., Gao, S. S., Zhao, D., & Liu, K. H. (2020). Mantle Structure and Flow Beneath an Early-Stage Continental Rift: Constraints From P Wave Anisotropic Tomography. *Tectonics*, *39*(2), e2019TC005590. https://doi.org/10.1029/2019tc005590